A Strong Constraint on Radiative Forcing of Well-mixed Greenhouse Gases

Jing Feng

jing.feng@princeton.edu

Princeton University https://orcid.org/0000-0003-1144-622X

David Paynter

GFDL

Raymond Menzel

Geophysical Fluid Dynamics Laboratory

Ryan Kramer

https://orcid.org/0000-0002-9377-0674

Physical Sciences - Article

Keywords: Radiative Forcing, Greenhouse Gases, Earth System Modeling

Posted Date: August 8th, 2025

DOI: https://doi.org/10.21203/rs.3.rs-7247389/v1

Additional Declarations: There is **NO** Competing Interest.

A Strong Constraint on Radiative Forcing of Well-mixed Greenhouse Gases

Jing Feng[1*], David Paynter[2], Raymond Menzel[2], Ryan Kramer[2]

[1*]Atmospheric and Oceanic Sciences Program, Princeton University, 300 Forrestal Road, Princeton, 08540, New Jersey, United States.
[2]Geophysical Fluid Dynamics Laboratory, 201 Forrestal Road, Princeton, 08540, New Jersey, United States.

*Corresponding author(s). E-mail(s): jing.feng@princeton.edu;
Contributing authors: david.paynter@noaa.gov; raymenzel1324@gmail.com; ryan.kramer@noaa.gov;

Abstract

Radiative forcing from well-mixed greenhouse gases (WMGHGs) is a primary driver of Earth's energy imbalance but remains difficult to constrain due to its dependence on atmospheric state and model discrepancies. We present the first global benchmark of longwave (LW) instantaneous radiative forcing (IRF) for major WMGHGs under realistic, all-sky conditions. This benchmark is supported by (1) global line-by-line radiative transfer simulations using 24 years of reanalysis-based atmospheric and cloud conditions, and (2) a robust linear relationship between LW IRF and outgoing longwave radiation, enabling direct observational constraints from satellites. Using this framework, we estimate that the rising WMGHG concentrations have increased LW IRF by $3.71 \pm 0.07 \mathrm{W/m^2}$ from 1850 to 2024. Applying this benchmark to Earth System Models, we reduce the uncertainty in CO_2 effective radiative forcing by 60%. This observation-informed, physically grounded method offers a more accurate and consistent constraint on greenhouse gas forcing for future climate assessment reports.

Keywords: Radiative Forcing, Greenhouse Gases, Earth System Modeling

Main

Earth's radiative energy balance is fundamentally regulated by greenhouse gases (GHGs), which absorb and re-emit infrared radiation, exerting a profound influence on the planet's climate system. Anthropogenic emissions of well-mixed greenhouse gases (WMGHGs), including CO_2, CH_4, N_2O, chlorofluorocarbons (CFCs) and hydroflouro-carbons (HFCs), perturb this balance by reducing outgoing longwave radiation (OLR), thereby inducing global warming until a new equilibrium is achieved. The magnitude of this perturbation is characterized by instantaneous radiative forcing (IRF), defined as an instantaneous change in net radiative fluxes at top-of-atmosphere (TOA) or tropopause [1–7].

Recent decades have brought major advances in our ability to constrain the radiative forcing of WMGHGs. Long-term gas concentration records from observational networks such as NOAA Earth System Research Laboratories (ESRL) and NASA Advanced Global Atmospheric Gases Experiment (AGAGE) [8, 9], combined with improvements in molecular spectroscopy and line-by-line radiative transfer modeling [10, 11], have enabled high-fidelity benchmark estimates of IRF for selected atmospheric profiles [12–14]. Under carefully sampled conditions, line-by-line calculations have provided high-confidence estimates of IRF for clear-sky (cloud free) conditions. For example, the most recent benchmark for the clear-sky longwave (LW) IRF due to WMGHG increases from 1850 to 2014 is 2.66 to 2.69 Wm^{-2} at TOA, and 3.63 to 3.66 Wm^{-2} at tropopause, with sampling errors below 0.015 Wm^{-2} relative to the 2014 climatology (Table S1)[14]. The benchmark has not been updated in a decade, despite substantial increases in WMGHG concentrations since 2014 [15].

Despite these advances, benchmark estimates of radiative forcing remain limited to fixed clear-sky background conditions and do not capture the broader uncertainties associated with evolving surface temperatures, stratospheric states, water vapor, and cloud distributions for CO_2 [16–21] and other WMGHGs [22–27]. Over 90% of

WMGHG IRF arises from the longwave (LW) spectrum [13, 14], where radiative fluxes are highly sensitive to background atmospheric conditions [28, 29]. line-by-line radiative transfer calculations using a limited set of observed cloud profiles can estimate all-sky IRF [13, 23], but sampling errors become more uncertain due to the spatio-temporal variability of clouds [30]. Moreover, when used as inputs to line-by-line calculations, persistent biases and uncertainties in humidity and cloud fields in reanalyses [31, 32] and Earth system models (ESMs) [29, 33] introduce additional uncertainties that are challenging to constrain.

In ESMs, the effective radiative forcing of WMGHGs remains uncertain by more than 12% [7, 34], with more substantial spread (∼15%) in the LW IRF component[17, 20, 35]. These uncertainties stem from both inter-model differences in atmospheric state representations [18, 20] and limitations in radiative parameterizations [14]. Although line-by-line methods applied to various evolving background states could clarify these inter-model differences, they remain computationally prohibitive.

Satellite measurements of radiance and irradiance show WMGHG forcing signatures [36, 37], but these signals intermingle with variability in surface temperature, water vapor, clouds, aerosols, and short-lived climate forcers. Isolating the greenhouse gas component requires radiative transfer simulations based on retrieved or assumed background conditions [36–40], introducing uncertainties often exceed 10%—comparable to or even greater than the inter-model spread. Although these observations provide compelling evidence of anthropogenic influence, they have not yet yielded robust quantitative constraints on IRF.

Together, these limitations underscore a central challenge: despite advances in spectroscopy, satellite observations, and radiative modeling, the state dependence of LW IRF remains a leading source of uncertainty in the radiative forcing of greenhouse gases.

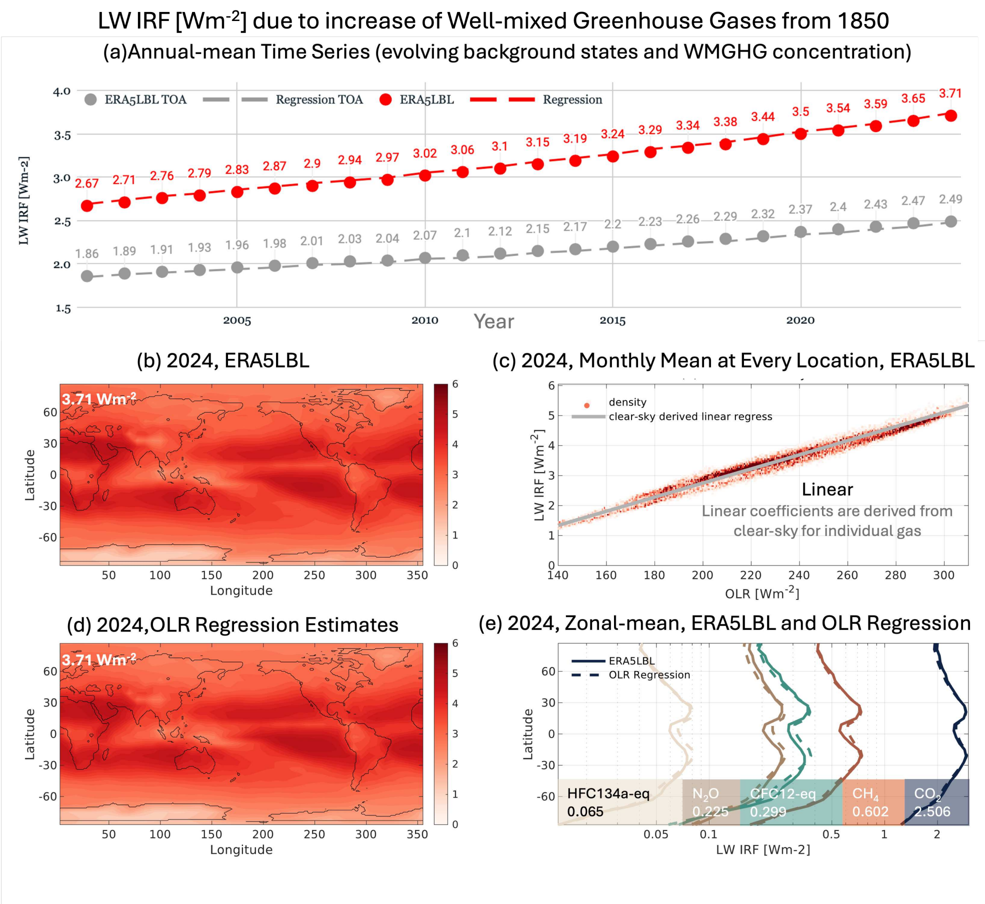

Fig. 1 Global line-by-line calculations reveal a strong linear relationship between LW IRF and OLR. This forms the basis of a regression model (Eq. 1, Table S2 and S3). Panel (a) shows the global annual-mean LW IRF (red: tropopause, gray: TOA) time series from ERA5LBL (solid) and regression estimates based on evolving WMGHG concentrations and OLR from ERA5LBL (dashed). Panels (b–e) evaluate LW IRF at the tropopause from WMGHG increases (1850–2024) under 2024 ERA5LBL background conditions: (b) annual-mean LW IRF from ERA5LBL; (c) joint histogram of monthly LW IRF (y-axis) and OLR (x-axis) compared with regression estimate from clear-sky relationships (gray); (d) LW IRF reconstructed from spatial OLR of ERA5LBL using the regression model; (e) zonal-mean LW IRF from ERA5LBL (solid) and regression applied to zonal-mean OLR of ERA5LBL (dashed) for major WMGHGs.

Global-Scale Line-by-Line Benchmark of Longwave Radiative Forcing

Enabled by the GPU-optimized line-by-line radiative transfer code (GRTcode) developed at NOAA's Geophysical Fluid Dynamics Laboratory, this study presents the first global-scale, decadal line-by-line calculations of longwave radiative forcing for CO_2, CH_4, N_2O, CFCs, and HFCs. The code is benchmarked by Pincus et al. (2020) [14]. These calculations use monthly-mean surface temperature, air temperature, water vapor, ozone, and cloud from the ERA5 reanalysis dataset [41]. Annual-mean WMGHG concentrations follow the Coupled Model Intercomparison Project Phase 7 (CMIP7) input datasets from 2001 to 2022 [9], with CO_2, CH_4, and N_2O extended to 2024 using NOAA ESRL trends [42, 43], as detailed in the *Methods*. Following Meinshausen et al. (2017)[8], radiative effects of ozone-depleting substances are combined as CFC-12 equivalence (CFC12eq), and other fluorinated gases as HFC-134a equivalence (HFC134a-eq). Results generated following this experiment setup is referred to as ERA5LBL.

The ERA5LBL dataset provides gridded, monthly-mean outgoing longwave radiation (OLR) from 2001 to 2024 for a 'Control' experiment. To isolate the LW IRF of WMGHG x, relative to pre-industrial (PI, 1850) concentrations, sensitivity experiments (xPI) are conducted that are identical to the Control experiment, except that gas x is held fixed at its PI concentration. Additional experiments are performed for doubled and quadrupled PI CO_2 concentrations. Details are provided in the Supplementary Materials (*Methods*). For each gas x, the LW IRF at vertical level i is computed as the difference in net downward LW flux between the Control and perturbation (xPI) experiments:

$$F_{i,x} = (R_{\downarrow,i,xPI} - R_{\uparrow,i,xPI}) - (R_{\downarrow,i,\mathrm{Control}} - R_{\uparrow,i,\mathrm{Control}}), \quad (1)$$

where $R_{\uparrow,i}$ and $R_{\downarrow,i}$ denote the upwelling and downwelling LW radiative fluxes at level i. While the IRF at the TOA is often used to decompose the TOA energy budget, the tropopause value is more relevant for surface temperature responses and adjusted forcing [1, 2, 5, 6, 44, 45]. In this paper, LW IRF at TOA is referred to as

IRF_{TOA}, and 'LW IRF' specifically refers to F_i at the **200 hPa** level [4], which serves as a consistent tropopause level for benchmark evaluations.

From 2001 to 2024, ERA5LBL simulations show an increase in LW IRF from 2.67 to 3.71 Wm^{-2}, and at TOA from 1.86 to 2.49 Wm^{-2} (Fig.1a). The increase in CO_2 from 370.8 to 423.0 parts per million by volume (ppmv) accounts for 0.853 Wm^{-2} of the increase, while CH_4, N_2O, HFC134a-eq, and CFC12-eq contribute 0.080, 0.073, 0.051, and -0.008 Wm^{-2}, respectively.

Compared to the recent benchmark by Pincus et al. (2020) [14], which estimated LW IRF_{TOA} from 100 ERA5 profiles in 2014, our global clear-sky LW IRF (3.64 Wm^{-2}) and LW IRF_{TOA} (2.67 Wm^{-2}) show excellent agreement (Table S1). Pincus et al. did not provide a benchmark for all-sky conditions but estimated LW IRF_{TOA} between 1.98 and 2.07 Wm^{-2}, based on the all-sky to clear-sky IRF ratio from three CMIP6 models [39, 46, 47]. Our ERA5LBL-derived all-sky LW IRF_{TOA} for 2014 is 2.17 Wm^{-2}, exceeding the upper bound of this range, suggesting weaker LW cloud effects in ERA5 than those CMIP6 models.

Alternative estimates of all-sky LW IRF can be obtained from simplified expressions [7, 12, 13] (Table S3), using conversion factors from line-by-line calculations with sampled cloud profiles [48, 49] (Table S4). Combining IPCC AR6[7] for CFCs/HFCs with Etminan et al. (2016)[13] for CO_2, CH_4, and N_2O gives 3.14 Wm^{-2} for 2014; using Byrne and Goldblatt (2014)[12] yields 2.99 Wm^{-2}. Both are lower than the ERA5LBL benchmark (3.19 Wm^{-2}), likely due to uncertainties in the conversion factors, simplified expressions, or cloud effects.

While ERA5 likely provides more realistic atmospheric and cloud conditions by assimilating all-sky satellite observations [41], potentially improving persistent biases in earlier reanalysis datasets [32], simulating cloud radiative effects in line-by-line models remains sensitive to assumptions about subcolumn cloud inhomogeneity [30, 50, 51], vertical cloud overlap [52, 53], and hydrometeor particle sizes [54–56]. These sensitivities lead to biases and uncertainties that are challenging to quantify.

Constraining Present-day Radiative Forcing Using Robust Linear Dependence on OLR

Despite potential uncertainties in all-sky forcing estimates, the LW IRF of different WMGHGs exhibits highly consistent spatial patterns (Fig.1b; see also Fig.S1), largely independent of cloud conditions. This consistency aligns with the inhomogeneous forcing structure previously identified for CO_2[18]. We find that the spatial variability in IRF closely follows local outgoing longwave radiation (OLR) under both clear-sky and all-sky conditions (Figs.S1-S2). This strong correspondence suggests that temperature, humidity, and clouds influence OLR[28, 29] and LW IRF in similar ways: IRF tends to be higher in regions with warmer surface temperatures [28] and lower where relative humidity or cloud amount is higher [29].

Motivated by this relationship, we construct a simple regression model for each WMGHG using ERA5LBL results under clear-sky conditions:

$$F = a(R - b) - r, \tag{2}$$

where F is the LW IRF, R is the clear-sky OLR under present-day WMGHG concentrations ("Control"; see *Methods*), and a and b are regression coefficients representing the slope and intercept (Fig.S3). The coefficients are derived under the constraint of zero global-mean bias in clear-sky IRF for the year 2010 ($r = 0$) and are summarized in Table S2.

This regression approach accurately reproduces the clear-sky LW IRF spatial pattern for all gases (Figures S2, for 24-year-average) and achieves global-mean accuracy comparable with five benchmark line-by-line models (Table S1)[14]. IRF induced by individual WMGHGs is additive, with a small global-mean residual of $-0.017\,\mathrm{Wm}^{-2}$ ($\sim 0.5\%$) in the year 2010.

Remarkably, this linear relationship remains the same under all-sky conditions. By substituting all-sky OLR into Equation 2, the clear-sky-derived regression model accurately predicts the all-sky LW IRF–OLR relationship (gray line in Fig.1c; $R^2 = 0.99$), the spatial distribution of LW IRF (Fig.1d), and the zonal-mean profiles for each gas (Fig.1e; dashed vs. solid curves). The global-mean bias (r in Eq.2) under all-sky conditions remains within $0.01\,\mathrm{Wm}^{-2}$ (Table S2). Further evaluations for individual gases and IRF_{TOA} results are provided in the *Methods* (Table S5, Figs. S3–S4).

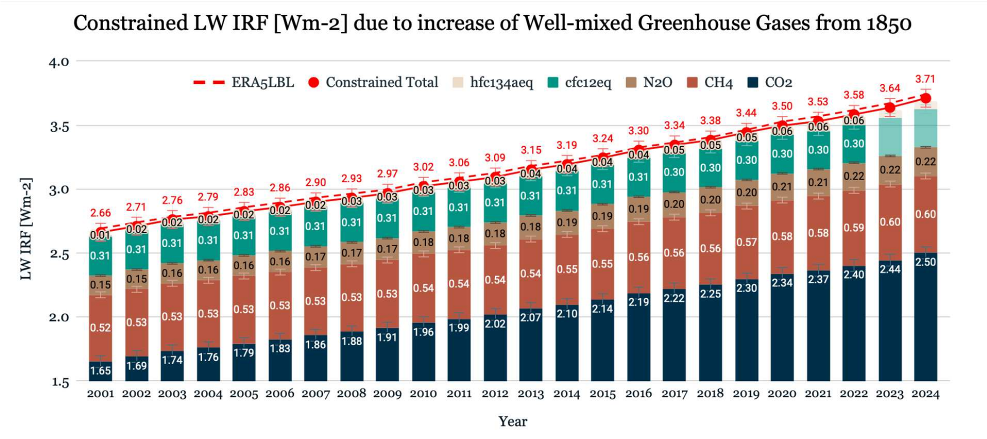

Fig. 2 Constrained LW IRF due to the increase in major WMGHG concentrations relative to 1850, based on clear-sky-derived linear coefficients from ERA5LBL, global-mean timeseries of OLR from CERES EBAF v4.2, and global-mean timeseries of WMGHG concentrations. LW IRF from all-sky ERA5LBL is shown as dashed red curve.

Applying this regression model to time-varying WMGHG concentrations and global-mean OLR from ERA5LBL yields excellent agreement with directly computed LW IRFs (dashed lines versus markers in Fig.1a). The 5–95% confidence range for the global annual-mean LW IRF is conservatively estimated at $0.064\,\mathrm{Wm}^{-2}$ ($\sim 2\%$), based on deviations from monthly, meridional-mean LW IRF between 2001 and 2024. This uncertainty range is valid as long as Earth's annual-mean climate state remains within the seasonal and meridional variability sampled by ERA5LBL, the envelope from which the regression coefficients were derived. Thus, the OLR-regression method enables the LW IRF to be estimated directly from observed OLR, independent of biases in atmospheric state variables and cloud radiative effects.

We apply this regression model to CERES EBAF v4.2 satellite observations of OLR [57] to produce observationally-constrained estimates of LW IRF relative to preindustrial levels. The OLR in the CERES EBAF product uses an objective constrainment algorithm [58] that adjusts radiation fluxes for consistency with heat storage in the Earth-atmosphere system; the remaining global-mean OLR uncertainty of $\pm$ 2.5 Wm^{-2} [57]. This yields annual time series of LW IRF for individual WMGHGs over 2001–2024 (Fig.2). Over this 24-year period, the CERES-constrained LW IRF for WMGHGs increases from **2.66 to 3.71** Wm^{-2} (2.66 to 3.66 Wm^{-2} if the background climate is fixed at 2001). The 5-95% uncertainty range is **0.073** Wm^{-2} ($\sqrt{0.064^2 + 0.015^2 + 0.032^2}$, including 0.064 Wm^{-2} from the regression method, 0.015 Wm^{-2} from clear-sky line-by-line calculations, and 0.032 Wm^{-2} from the uncertainty in OLR; see Fig. S5 and S6 for a breakdown of the uncertainty related to each WMGHG).

These observationally constrained estimates enable a direct comparison with LW IRF derived independently from the cloud effects represented by ERA5LBL. Because OLR in ERA5LBL is highly consistent with CERES EBAF v4.2, the CERES-constrained values achieve excellent agreement with those computed from ERA5LBL. This agreement reinforces confidence in our ERA5LBL calculations for LW IRF.

Implications to Earth System Modeling

In Earth system models (ESMs), effective radiative forcing (ERF) with fixed sea surface temperature (F_{fsst}) is diagnosed as the TOA energy imbalance following rapid atmospheric adjustments to greenhouse gas perturbations. These values are commonly reported for $2\times CO_2$ and $4\times CO_2$ scenarios and serve as essential metrics for quantifying equilibrium climate sensitivity [7]. In IPCC AR6 [7], F_{fsst} was reported as 3.71 $\pm$ 0.44 Wm^{-2} for $2\times CO_2$ and 7.98 $\pm$ 0.76 Wm^{-2} for $4\times CO_2$, based on multi-model CMIP6 results [59].

In some ESMs, the IRF can be diagnosed using a second radiation call at every model timestep, for which absorber concentrations are perturbed while all other model fields remain unchanged. The fluxes from this diagnostic-only "double-call" do not feed back on the model physics and represent the instantaneous response to the specified forcing agent. For WMGHGs, such double-call perturbations are available only for $4\times CO_2$ in AMIP experiments [60], and only for a limited subset of six ESMs. As a result, $4\times CO_2$ is currently the only scenario for which IRF can be directly diagnosed in these models. Because ESMs must rely on computationally efficient radiation parameterizations rather than spectrally resolved line-by-line radiative transfer, such double-call diagnostics provide a critical means of evaluating how well the internal radiation scheme of each model captures the intended forcing response.

Using the double-call diagnostics from the six ESMs and corresponding ERF values from AMIP-$4\times CO_2$ simulations (Table S6), we find that ERF (8.10 $\pm$ 1.12 Wm^{-2}) strongly correlates with LW IRF (8.75$\pm$1.26 Wm^{-2}, $R^2 = 0.91$, Fig.3a), but shows a much weaker correlation with IRF_{TOA} ($R^2 = 0.48$, Table S6). Thus the LW IRF is a dominant cause of spread in ERF across these models.

To trace the source of inter-model spread in LW IRF, we conduct offline radiative transfer simulations using monthly-mean atmospheric conditions from each model, as described in the *Methods*. These simulations are performed under clear-sky conditions using a fast RTE-RRTMGP parameterization code [61], which isolates radiative responses from the model-specific representations of cloud processes. A known +0.33 Wm^{-2} bias in RTE-RRTMGP has been removed following benchmark studies [14]. The resulting LW IRF values exhibit good agreement across models (black points, x-axis of Fig.3b), with a spread of only 0.2 Wm^{-2}, much smaller than the 1.26 Wm^{-2} spread seen in double-call diagnostics. Importantly, this spread is not driven by clouds: the variability under clear-sky double-call diagnostics (blue) is nearly identical to that in all-sky (yellow), indicating that discrepancies arise mainly from differences in radiation parameterizations.

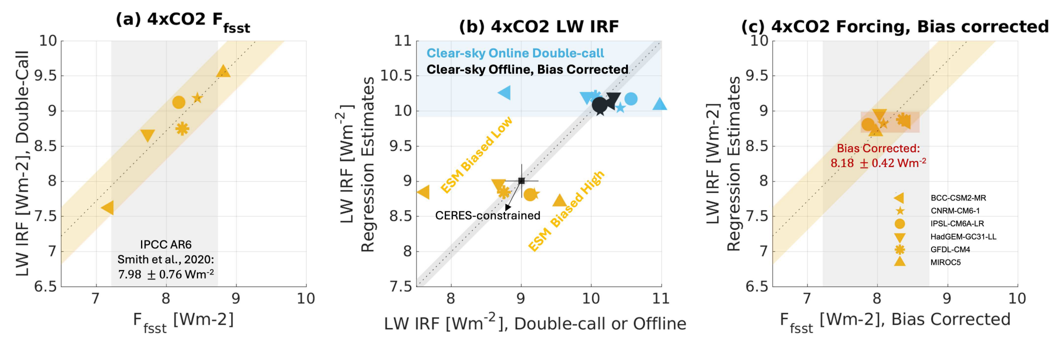

Fig. 3 Evaluation of $4\times CO_2$ radiative forcing in Earth System Models (ESMs). (a) Comparison of $4\times CO_2$ effective radiative forcing (F_{fsst}, x-axis) and longwave instantaneous radiative forcing at tropopause (LW IRF, y-axis) from online double radiation call diagnostics.(b) Comparison of LW IRF simulated by online double radiation call (x-axis; yellow: all-sky, blue: clear-sky), clear-sky offline RTE-RRTMGP with 0.33 Wm^{-2} bias correction applied (x-axis, black) [14], and estimates from the regression method applied to the simulated OLR (y-axis). CERES-constrained LW IRF from 8.95 to 9.06 $\pm Wm^{-2}$ over the 2001 to 2024 time period is shown as a black square. (c) Same as (a), but with model-specific bias corrections to LW IRF based on panel (b).

Although line-by-line calculations under all-sky conditions could, in principle, provide benchmark LW IRF estimates for each model, such calculations are computationally prohibitive and cannot realistically represent the model-specific cloud–radiation interaction processes. Instead, our regression framework offers a computationally efficient alternative, enabling accurate estimates of LW IRF across a broad range of atmospheric and cloud states as described by the OLR of these models.

Similar to previous sections, we derive the regression model for LW IRF $4\times CO_2$ based on clear-sky ERA5LBL calculations of OLR at pre-industrial CO_2 ('CO_2PI',

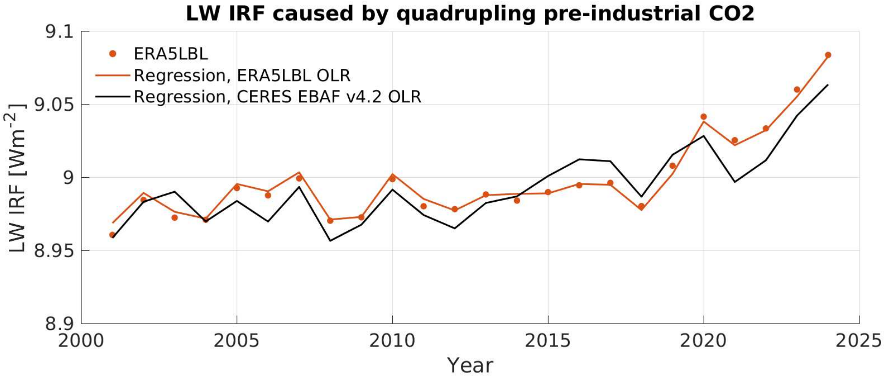

Fig. 4 LW IRF of $4\times CO_2$ (with respect to pre-industrial levels) at evolving background states from 2001 to 2024 from ERA5LBL (red scatters), the estimates from the regression applied to ERA5LBL OLR (red curve), and the estimates from the regression applied to CERES EBAF v4.2 OLR (black).

Methods) and calculations of LW IRF from quadrupled pre-industrial CO_2 ('$CO_2$4xPI', *Methods*) as:

$$F_{4\times CO_2} = 0.0509(R_{CO_2PI} - 63\ \mathrm{Wm}^{-2}) - r, \tag{3}$$

where R_{CO_2PI} represents the OLR if CO_2 were returned to 1850 levels while all other atmospheric variables remained at present-day conditions. This quantity is reconstructed as the sum of present-day OLR and the estimated LW IRF_{TOA} from CO_2 increase since 1850, for which the IRF_{TOA} is derived using the regression method (Table S5; evaluated in Figs. S4, S6). Our formulation uses pre-industrial levels, consistent with IPCC assessments. The global-mean bias evaluated at year 2010 is $r = 0.095\mathrm{Wm}^{-2}$ (Table S2), and the 5–95% confidence interval is assessed to be $\pm 0.10\ \mathrm{Wm}^{-2}$ using the 24-year monthly-mean, global-mean as described earlier. This regression-based uncertainty is smaller than the spread across five independent line-by-line models (0.19 Wm^{-2}, Table S1). In Fig.4, we apply this method to R_{CO_2PI} values derived from both ERA5LBL and CERES and have achieved excellent agreement. When using CERES-based global-mean OLR, the regression method estimates that LW IRF increases from 8.96 Wm^{-2} in 2001 to $9.06\pm 0.24\ \mathrm{Wm}^{-2}$ in 2024, driven by record-high OLR observed in the past two years due to surface warming [15] and weakened cloud LW effects. The accuracy of these estimates under anomalous OLR conditions demonstrates the robustness of the regression method in a changing climate.

Differences between the regression estimates and IRF from model double-call diagnostics provide a direct measure of radiation parameterization biases in ESMs. We show that the regression technique explains the clear-sky LW IRF simulated by the bias-corrected clear-sky offline calculations very well (Fig.3b, black, for six experiments with double-call diagnostics; Fig.S7 for experiments without double-call). Extending the regression to all-sky OLR from the double-call diagnostics of ESMs (Fig.3b, y-axis), we find that the all-sky LW IRF of these models is 8.87±0.16Wm^{-2}, close to the CERES-constrained range of 8.95 to 9.06±0.24 Wm^{-2}. This reduced inter-model spread reflects that ESMs agree well with observed global-mean OLR during the historical period. Deviations from regression values are interpreted as model-specific radiation biases. Assuming the reduced uncertainty in IRF can translate to an equivalent reduction in ERF uncertainty, we derive a bias-corrected F_{fsst} of 8.18±0.42 Wm^{-2} (Fig.3c) for 4×CO2, significantly narrower than the original spread of 8.10± 1.12 Wm^{-2}. This correction reduces inter-model spread in F_{fsst} by 60%.

The remaining uncertainty (yellow shading in Fig.3b) likely reflects differences in shortwave forcing [13, 26, 49], adjustment processes [34, 59], and base-state conditions [20]. As these processes are not fully independent of radiation, it is possible to achieve a further reduction in inter-model spread if the same radiation parameterizations are adopted.

Conclusion

This study establishes the first global benchmark for the LW IRF of WMGHGs under realistic, all-sky conditions. Using a spectrally resolved, highly parallelized line-by-line radiative transfer model, we quantify a post-1850 LW IRF of 3.71±0.07 Wm^{-2} by 2024, with 38% of this increase occurring since 2001. Confidence in this benchmark is reinforced by a regression method that integrates observational constraints from satellite-observed OLR to account for uncertainties from cloud effects and evolving climate states.

We further demonstrate that IRF values can be accurately derived from the OLR-regression method applied to ESMs, offering a practical alternative to computationally intensive line-by-line diagnostics for benchmarking climate projections. Applying this framework reduces the uncertainty in CO_2-induced effective radiative forcing by over half compared to the IPCC Sixth Assessment Report and provides a scalable pathway for evaluating forcing across all major WMGHGs. A community-wide adoption of this framework would strengthen the physical consistency of climate assessments and enhance confidence in long-term climate projections.

Acknowledgements. We acknowledge computation resources from GFDL and Princeton CIMES made available for this research. This report was prepared by Jing Feng under award from the National Oceanic and Atmospheric Administration, U.S. Department of Commerce. The statements, findings, conclusions, and recommendations are those of the author(s) and do not necessarily reflect the views of the National Oceanic and Atmospheric Administration, or the U.S. Department of Commerce. We acknowledge Vaishali Naik, Chongxing Fan and Arman Pouyaei for their detailed and constructive internal review of this study.

Methods

Line-by-line Calculations

The Geophysical Fluid Dynamics Laboratory's GPU-compatible radiation code (GRTcode) is a line-by-line radiative transfer code using HITRAN 2016 [10] and MT_CKD 2.5 [62]. It has been benchmarked in Pincus et al. (2020) [14], showing excellent agreement with other line-by-line radiative transfer models including LBLRTM v12.8 [63] provided by Atmospheric and Environmental Research, RFM [64] calculation conducted by Geophysical Fluid Dynamics Laboratory, 4AOP [65] provided by the Laboratoire de Météorologie Dynamique, ARTS 2.3 [66] provided by the University of Hamburg. We also note that although GRTcode does not include CO_2 line mixing, it agrees well with models (such as RFM and LBLRTM) that include the mechanism, which is consistent with the understanding that the line mixing induces negligible (within 1%) impacts on the longwave radiative forcing [11]. Details of this comparison are listed in Table S1. Inter-model discrepancies are estimated as the standard deviations and are multiplied by 1.96 to infer 5-95% of uncertainty in IRF caused by gas spectroscopy.

For clouds, the GRTcode adopts a high spectral resolution cloud optics parameterization developed by Feng et al., 2025 [56], which has been validated to achieve reasonable radiative closure with hyperspectral resolution remote sensing instruments in the mid-infrared [67, 68]. The cloud optics parameterization [56] is built upon Mie-scattering calculations for liquid clouds and an optics library for severely roughened solid columns developed by Yang et al. (2013) [69]. Based on grid-cell-mean cloud fraction and cloud water content, subgrid cloud water content is stochastically generated at every wavenumber following Pincus et al., 2006 [30], and cloud optical depth is assumed to be uniform within each 1 cm^{-1} bin. The all-sky calculations of GRTcode, with broadband cloud optics parameterizations, have shown good agreement in

Table S1 Clear-sky LW IRF [Wm^{-2}] from five line-by-line models [14] with respect to 100 profiles sampled from reanalysis products at year 2014. Standard deviations across these models are used to infer 5-95% uncertainty range in the line-by-line calculation of IRF. The OLR-regression method ('Regress') is applied using multi-model-mean clear-sky OLR and gas concentrations from Pincus et al., 2020 [14]. The ERA5LBL results for the global-mean of 2014 are listed based on an updated gas concentration datasets following CMIP7.

Scenario	4AOP	ARTS	**GRTcode**	RFM	LBLRTM	**Mean/STD**	**Regress**	ERA5LBL
OLR baseline	263.14	261.94	262.95	263.25	263.20	**262.90/0.55**	-	261.90
				LW IRF at 200 hPa tropopause				
2014-1850 CO_2	2.39	2.36	2.38	2.38	2.42	**2.38/0.02**	**2.38**	2.37
2014-1850 CH_4	0.64	0.64	0.64	0.64	0.64	**0.64/0.01**	**0.65**	0.65
2014-1850 N_2O	0.21	0.21	0.21	0.21	0.21	**0.21/0.01**	**0.21**	0.22
2014-1850 CFC+HFC	0.42	0.42	0.42	0.41	0.38	**0.41/0.02**	**0.43**	0.43
4×CO_2	10.26	10.15	10.20	10.23	10.40	**10.25/0.10**	**10.22**	10.17
				LW IRF_{TOA}				
2014-1850 CO_2	1.30	1.31	1.29	1.29	1.32	**1.30/0.01**	**1.31**	1.29
2014-1850 CH_4	0.62	0.61	0.62	0.62	0.61	**0.61/0.01**	**0.62**	0.62
2014-1850 N_2O	0.21	0.21	0.20	0.21	0.21	**0.21/0.01**	**0.21**	0.21
2014-1850 CFC+HFC	0.57	0.56	0.56	0.55	0.50	**0.55/0.03**	**0.56**	0.56
4×CO_2	5.40	5.45	5.32	5.37	5.51	**5.41/0.08**	**5.38**	5.33

long-term global-mean trend with space-borne hyper-spectral infrared sounders [40]. Using annual-mean, monthly-mean surface temperature, humidity, ozone concentration, and cloud conditions from the ERA5 [41] reanalysis dataset at 2.5° resolution, a set of global-scale line-by-line experiments perturbing the concentrations of well-mixed greenhouse gases (WMGHGs) was conducted for the period 2003–2022. These experiments include:

- Control: A control experiment using a time series of global-mean, annual-mean concentrations of WMGHGs [9].
- xPI: Identical to Control, except that an individual WMGHG species, x, is held fixed at its 1850 concentration (CO_2 : 284.297 parts per million by volume (ppmv), CH_4 : 0.7988 ppmv, N_2O : 0.2716 ppmv, 8.2×10^{-6} ppmv for CFC12eq and 2.02×10^{-5} ppmv HFC134a-eq).
- CO_2 4xPI: Similar to CO_2 PI, except that CO_2 concentration is four times of 1850 concentration.

These experiments generate top-of-atmosphere outgoing longwave radiation (OLR, Wm^{-2}). For the period from 2001 to 2022, the time series of WMGHG concentrations is based on the Climate Model Intercomparison Project Phase 7 (CMIP7) greenhouse input dataset [9]. For the years 2023 and 2024, global-mean concentrations of CO_2, CH_4, and N_2O are taken from NOAA's Global Monitoring Laboratory [42, 43], with a bias correction applied to ensure continuity with Nicolls et al., 2025 [9]. Concentrations of CFC-12-eq and HFC-134a-eq gases after 2022 are held fixed at their 2022 levels. Radiative transfer calculations are conducted at 0.1 cm^{-1} resolution; we have performed tests to demonstrate that increasing the resolution does not alter the broadband IRF. Table 1 lists the clear-sky LW IRF estimated from ERA5LBL calculations for the year 2014, the difference between the GRTcode results submitted to Pincus et al., 2020 [14] is minor and comes from samplings and differences in gas concentrations that have been updated since CMIP6.

The Linear OLR-Regression Method

We find that the monthly-mean, gridded LW IRF of WMGHGs is largely a linear function of OLR (Fig.S3), with linear coefficients closely matching those derived from cloud-free ('clear-sky') simulations. Using the ERA5LBL simulation for the year 2010 and a first-order linear regression model (Equation 2), we derive coefficients (a and b) from clear-sky simulations for both LW IRF and LW IRF at the top of the atmosphere (IRF_{TOA}, Fig.S4), yielding zero global-mean bias (r). The global-mean bias under all-sky conditions is then obtained by applying these coefficients to the all-sky OLR of the same year. For LW IRF resulting from increases in WMGHG concentrations relative to 1850 levels, the bias is within 0.02 Wm^{-2}; for $4\times CO_2$, the bias is 0.09 Wm^{-2}. These coefficients and biases are summarized in Table S2 (LW IRF) and Table S5 (LW IRF_{TOA}) and are held fixed for each forcing scenario.

Table S2 Regression coefficients for instantaneous longwave radiative forcing of WMGHGs at tropopause. The forcing follows the form $F = a(R - b) - r$, where R is the outgoing longwave radiation (OLR). The coefficient a is a function of gas concentration (ppmv), where C_0 and C are unperturbed and perturbed concentrations, following logarithmatic dependence for CO_2 [70], square-root dependence for CH4 and N2O [13], and linear dependence for CFCs and HFCs [22]. The term r is the global-mean bias in all-sky IRF (0 $\mathrm{Wm^{-2}}$ in clear-sky). These regression coefficients are derived from clear-sky monthly-mean, gridded ERA5LBL results at year 2010 and are evaluated using all-sky monthly-mean meridional-mean, providing the 5-95% uncertainty of the regression method.

Gas	a	b ($\mathrm{Wm^{-2}}$)	r ($\mathrm{Wm^{-2}}$)	5-95%
	Applied to OLR with present-day WMGHG concentrations			
CO_2	$0.0358\ln(C/C_0) + 0.0014\ln(C/C_0)^2$	63.0	0.015	1.2%
CH_4	$0.0089(\sqrt{C} - \sqrt{C_0}) - 0.0008(\sqrt{C} - \sqrt{C_0})^2$	110.0	0.007	4.0%
N_2O	$0.027(\sqrt{C} - \sqrt{C_0})$	100.0	0.004	3.3%
CFC-12eq	$2.77(C - C_0)$	124.0	0.016	6.6%
HFC-134aeq	$1.46(C - C_0)$	124.0	0.002	8.1%
Sum			0.017	
	Applied to OLR with pre-industrial CO_2 and present-day other WMGHGs			
$4 \times CO_2$	0.0509	63.0	0.095	1.0%

Table S3 All-sky LW IRF [$\mathrm{Wm^{-2}}$] caused by increases in major WMGHGs from 1850 to 2014. Estimates from Etminan et al. (2016) [13] and IPCC AR6 [7] are converted from net stratospherically adjusted radiative forcing (SARF) using conversion ratios in Table S3 (second column). Estimates from Byrne and Goldblatt (2014) [12] are converted from net IRF using Table S3 (third column). CERES-constrained LW IRF based on the OLR-regression methods are also shown for comparison.

Source	**Gas**	**Net SARF** [$\mathrm{Wm^{-2}}$]	**LW IRF**[$\mathrm{Wm^{-2}}$]	**Constrained LW IRF** [$\mathrm{Wm^{-2}}$]
Etminan et al. (2016) [13]	CO_2	1.806	2.059	2.097 ± 0.05
	CH_4	0.566	0.521	0.548 ± 0.02
	N_2O	0.175	0.173	0.187 ± 0.006
IPCC AR6 Ch.7 Supp. [7]	CFC12-eq	0.358	0.322	0.306 ± 0.039
	HFC134a-3q	0.040	0.036	0.038 ± 0.005
		Net IRF [$\mathrm{Wm^{-2}}$]		
Byrne & Goldblatt (2014) [12]	CO_2	1.830	1.922	2.097 ± 0.05
	CH_4	0.525	0.515	0.548 ± 0.02
	N_2O	0.198	0.198	0.187 ± 0.006

The linear regression model explains more than 90% of the monthly gridded variability in LW IRF and LW $\mathrm{IRF_{TOA}}$, except for LW $\mathrm{IRF_{TOA}}$ of CO_2 (Fig.S3-S4). This exception arises because LW $\mathrm{IRF_{TOA}}$ is sensitive to stratospheric temperature [19–21], which exhibit strong seasonal variations driven by the Brewer–Dobson circulation

Table S4 Conversion ratios from SARF or net IRF to LW IRF for major WMGHGs. References are listed in the left column for each gas.

Gas	LW IRF / Net SARF	LW IRF / Net IRF
CO_2 [13, 49]	1.14	1.05
CH_4 [13, 49]	0.92	0.98
N_2O [13, 14, 49]	0.99	1.00
CFC [4, 48]	0.90	–
HFC [4, 48]	0.90	–

[71]. On the other hand, the LW IRF used in this study, defined at the tropopause, is largely insensitive to stratospheric temperature and is therefore better captured by the regression model. This tropopause-based IRF is more closely aligned with the radiative forcing after stratospheric adjustment, which is primarily governed by radiative balance and provides a more robust indicator of surface climate change [6]. It has been adopted as the key metric for IRF since the first Intergovernmental Panel on Climate Change (IPCC) report [2, 4, 5]. Its importance is underscored by the strong correlation with the effective radiative forcing under fixed sea surface temperature (F_{fsst}), showing an R^2 of 0.91 (Fig.3a, Table S4). In contrast, the correlation between LW $\mathrm{IRF}_{\mathrm{TOA}}$ and F_{fsst} is much weaker, with an R^2 of 0.48 (Table S4).

The linear regression model is then applied to OLR from ERA5LBL for 24 years, accurately reproducing both spatial and zonal-mean patterns in LW IRF for each WMGHG (Figs. S1-S2). For CO_2 -induced LW $\mathrm{IRF}_{\mathrm{TOA}}$, for which state-dependent analytical models have been developed [17, 19, 72], our linear model explains 97% of the annual-mean gridded variability, outperforming more complex models. For monthly-mean meridional mean LW IRF, the 5–95% uncertainty range of the OLR-regression method for each WMGHG (Figs. S5-S6) generally falls within 2% of the IRF, which is comparable with the spread of line-by-line calculations as reported by Pincus et al. (2020) [14]. The total uncertainty (σ) when using observed OLR is computed as:

$$\sigma = \sqrt{\sigma_r^2 + a^2\sigma_o^2 + \sigma_s^2} \quad (1)$$

where σ_r is the regression uncertainty, σ_o is the uncertainty from CERES EBAF v4.2 OLR, and σ_s is the line-by-line calculation uncertainty as summarized in Table S2 [14]. These are assumed to be independent and are combined in quadrature. Sources of uncertainty are indicated in Figs.2, S5-S6. While the annual mean and 4xCO_2 LW IRF have been presented in the main text, the LW IRF_{TOA} is evaluated to be 2.15±0.08 Wm^{-2} for the 24-year average of WMGHG forcing relative to 1850 and 4.18±0.26 Wm^{-2} for 4xCO_2 .

Table S5 Similar to Table 1 but for LW IRF_{TOA}.

Gas	a	b (Wm^{-2})	r (Wm^{-2})
Applied to OLR with present-day WMGHG concentrations			
CO_2	$0.0359\ln(C/C_0)$	155.0	0.007
CH_4	$0.0118(\sqrt{C}-\sqrt{C_0})ppmv^{-1/2}$	148.0	-0.010
N_2O	$0.0366(\sqrt{C}-\sqrt{C_0})ppmv^{-1/2}$	148.0	-0.003
CFC-12eq	$4.25(C-C_0)ppmv^{-1}$	148.0	-0.001
HFC-134aeq	$2.40(C-C_0)ppmv^{-1}$	148.0	0.003
Sum			-0.014
Applied to OLR with pre-industrial CO_2 and present-day other WMGHGs			
$4\times CO_2$	0.0493	155.0	0.108

RTE-RRTMGP Calculations with ESM inputs

RTE-RRTMGP [61] is a Fortran library for fast global-scale radiative transfer calculations. As described in Feng et al., (2023) [29], radiative transfer simulations at every model grid are conducted with inputs of monthly-mean surface temperature, temperature and humidity profiles from standard CMIP6 outputs at 19 pressure levels, climatological ozone profile, and present-day WMGHG concentrations except for

CO_2 . Simulations are conducted with 1850 CO_2 concentrations and 4xCO_2 concentrations for 28 model runs conducted by 11 CMIP6 models for three experiments (piClim-control, piClim-4xCO_2, AMIP [60]), providing level-by-level downwelling and upwelling longwave radiative fluxes. These radiative fluxes are used to interpret the global-mean clear-sky OLR and LW IRF at each vertical level.

The radiative biases of RTE-RRTMGP can be evaluated using RFMIP [14] by comparing with line-by-line simulations for the same set of atmospheric profiles. The clear-sky LW IRF of 4xCO_2 simulated by RTE-RRTMGP is 10.536 Wm^{-2}, 0.33 Wm^{-2} higher than that by GRTcode for the same set of atmospheric profiles in Pincus et al., 2020 [14]. This bias is removed in Figure 3(b) and Figure S7 when compared to IRF estimated by the OLR-regression method. While results for AMIP experiments are included in Figure 3 as black, other experiments are included in Figure S7 further confirming that the OLR-regression method is able to estimate the clear-sky LW IRF accurately within the proposed uncertainty range (0.1 Wm^{-2}, based on evaluations conducted in Figure S5).

Table S6 Radiation flux diagnostics [Wm^{-2}] based on online double-radiation call of AMIP of six models, including BCC-CSM2-MR, CNRM-CM6-1, IPSL-CM6A-LR, MIROC5, GFDL-CM4, and HadGEM-GC31-LL. F_{fsst} is calculated as the net TOA radiation difference between AMIP and AMIP-4xCO_2 of the same model.

Variable	BCC	CNRM	IPSL	MIROC5	GFDL	HadGEM	Mean / Std
F_{fsst}	7.18	8.44	8.18	8.81	8.23	7.73	8.10 / 0.57
OLR	238.65	238.20	237.94	235.89	238.54	241.04	238.38 / 1.50
LW $\mathrm{IRF}_{\mathrm{TOA}}$	6.72	4.23	4.09	4.39	3.50	4.08	4.50 / 1.13
$F_{\mathrm{fsst}} = \mathrm{LW\ IRF} + \mathrm{SW\ IRF} + \mathrm{Adj}$							
LW IRF	7.62	9.19	9.13	9.55	8.75	8.67	8.82 / 0.67
SW IRF	-0.14	-0.69	-0.84	-0.56	-0.48	-0.39	-0.52 / 0.24
Adj	-0.30	-0.06	-0.11	-0.17	-0.04	-0.55	-0.20 / 0.19
LW IRF (Regression)	8.85	8.83	8.81	8.71	8.84	8.97	8.84 / 0.08
Radiation bias	1.23	-0.36	-0.31	-0.84	0.09	0.69	0.08 / 0.71
F_{fsst} (bias corrected)	8.41	8.08	7.87	7.98	8.32	8.42	8.18 / 0.21

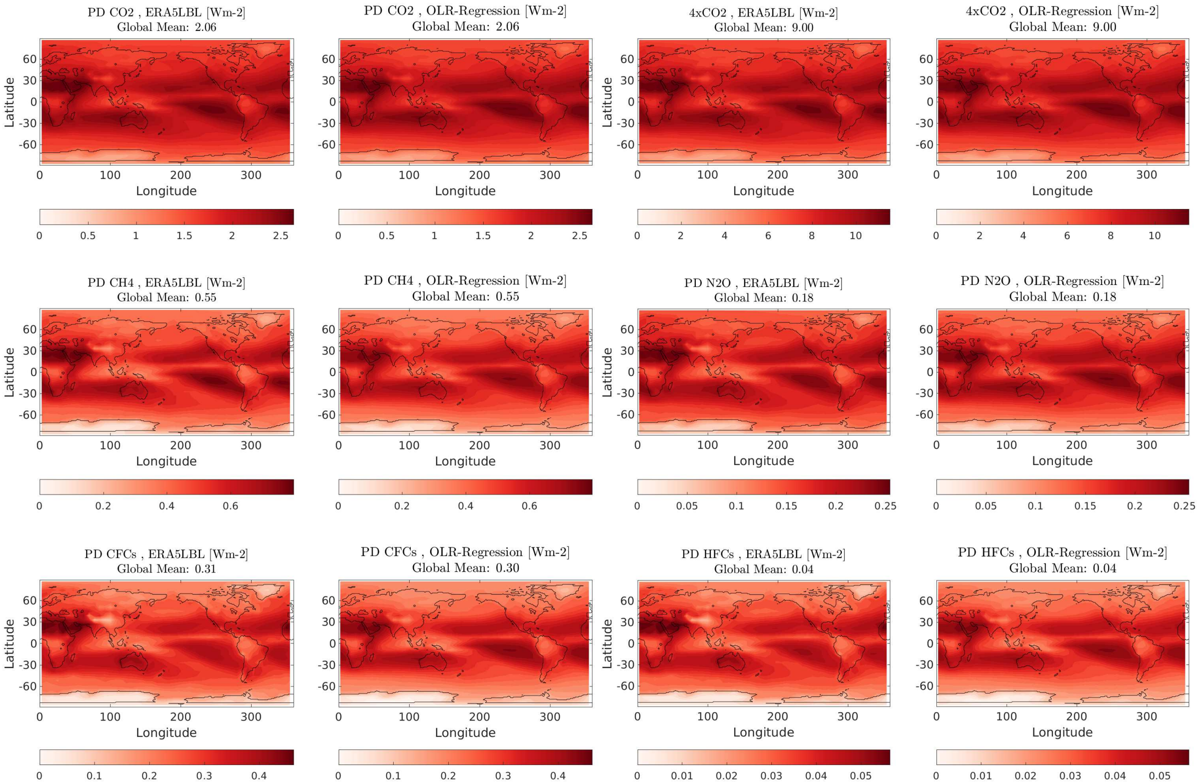

Fig. S1 Change in present-day (PD) (24-year mean, 2001 to 2024) LW IRF relative to the year 1850 caused CO_2, CH4, N2O, CFCs,HFCs, and 4xCO_2, from ERA5LBL and the regression estimates based on OLR simulated by ERA5LBL.

Declarations

- Data availability

Well-mixed greenhouse gas concentrations and radiative fluxes from ERA5LBL are available for all experiments listed in Supplementary Information at https://doi.org/10.5281/zenodo.15734292. CMIP6 and CMIP5 experiments are accessible via https://aims2.llnl.gov/search and summarized in *Methods*.

- Code availability

The GFDL line-by-line radiative transfer code is publicly accessible via https://github.com/fengzydy/GRTCODE/tree/All-skyIRF.

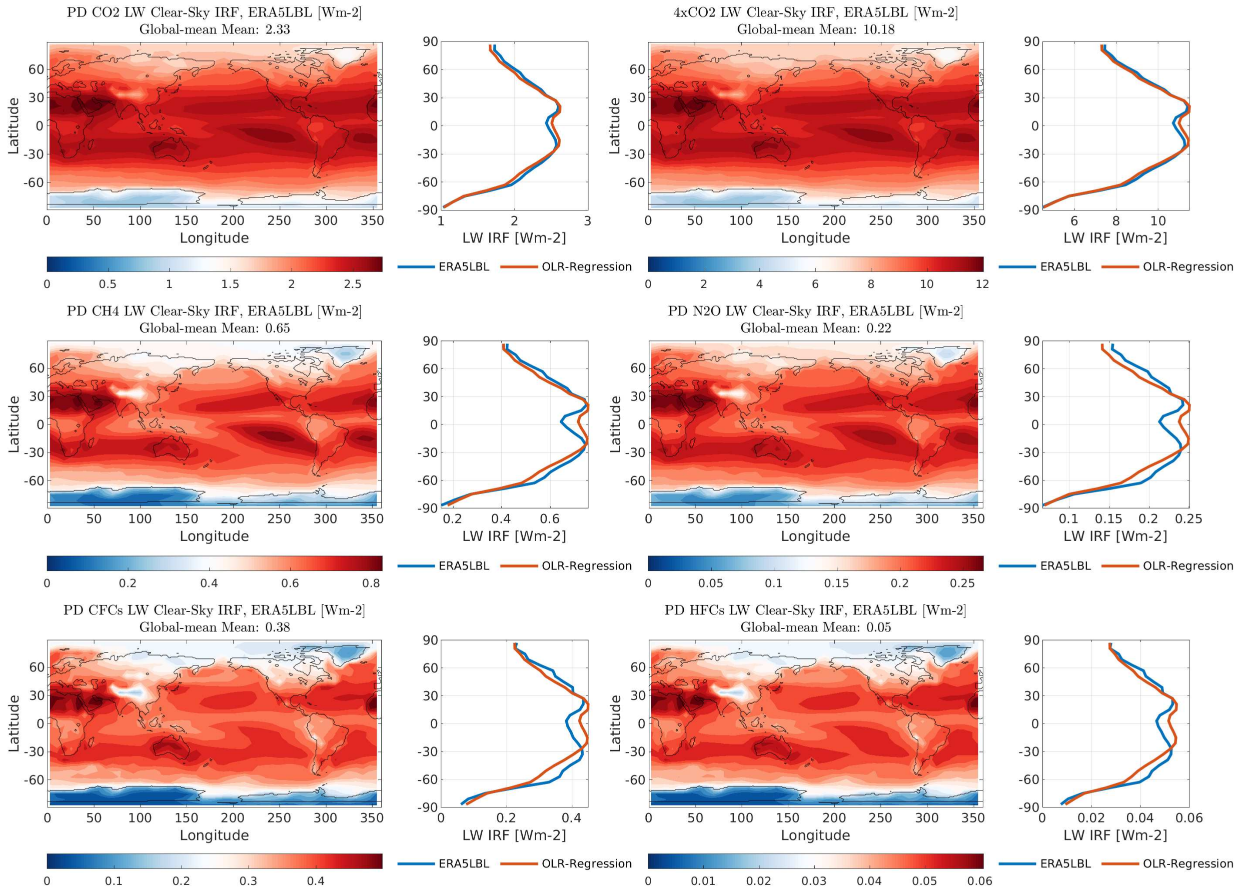

Fig. S2 The same as Figure S1 except for clear-sky IRF. Right panels of each figure compares the zonal-mean clear-sky obtained from the ERA5LBL (blue) and the OLR-regression method (red).

- Author contribution

J.F. and D.P. conceived the research project. J.F. conducted the line-by-line calculations and designed the regression framework. R.M. and J.F. developed the GRTcode. J.F. and R.K. contributed to data processing and analyzes. All authors contributed to the manuscript writing.

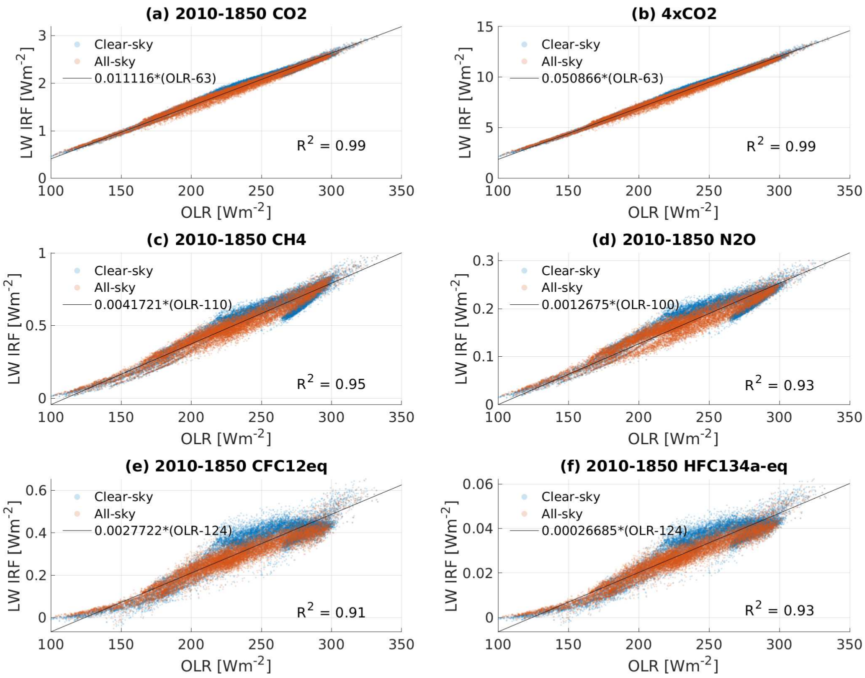

Fig. S3 Monthly gridded LW IRF as a function of OLR of the same location for (a) CO_2, (b) $4{\times}CO_2$, (c) CH4, (d) N2O, (e) CFC-12 equivalent, and (f) HFC-134a equivalent, each relative to preindustrial (1850) concentrations. Linear regression coefficients (Table S1) are derived from clear-sky ERA5LBL (blue), while biases and R^2 values are evaluated using all-sky ERA5LBL (red). Each scatter point represents a monthly-mean value for a grid cell from the ERA5LBL calculations at the year 2010.

References

[1] Fels, S., Mahlman, J., Schwarzkopf, M. & Sinclair, R. Stratospheric sensitivity to perturbations in ozone and carbon dioxide- radiative and dynamical response. *Journal of the Atmospheric Sciences* **37**, 2265–2297 (1980).

[2] Shine, K. P., Derwent, R., Wuebbles, D., Morcrette, J.-J. & Apling, A. in *Radiative forcing of climate* 41–68 (Cambridge University Press, 1990).

[3] Griggs, D. J. & Noguer, M. Climate change 2001: the scientific basis. contribution of working group i to the third assessment report of the intergovernmental panel

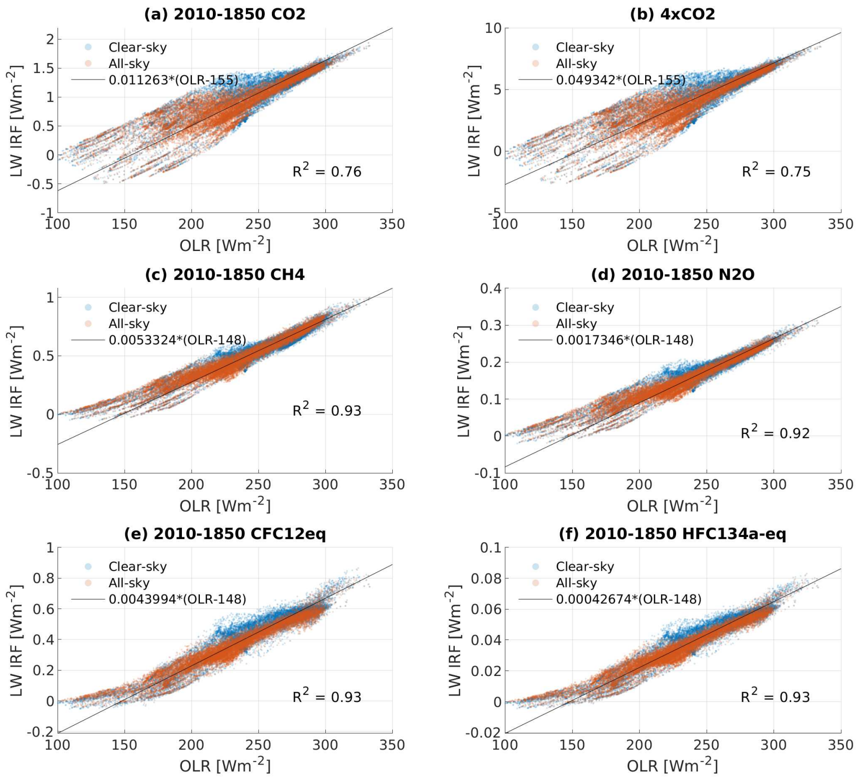

Fig. S4 Same as Fig.S3 but for LW IRF_{TOA}.

on climate change. *Weather* **57**, 267–269 (2002).

[4] Collins, W. *et al.* Radiative forcing by well-mixed greenhouse gases: Estimates from climate models in the intergovernmental panel on climate change (ipcc) fourth assessment report (ar4). *Journal of Geophysical Research: Atmospheres* **111** (2006).

[5] Myhre, G. *et al.* in *Anthropogenic and natural radiative forcing* (eds Stocker, T. F. *et al.*) *Climate Change 2013: The Physical Science Basis. Contribution of Working Group I to the Fifth Assessment Report of the Intergovernmental Panel*

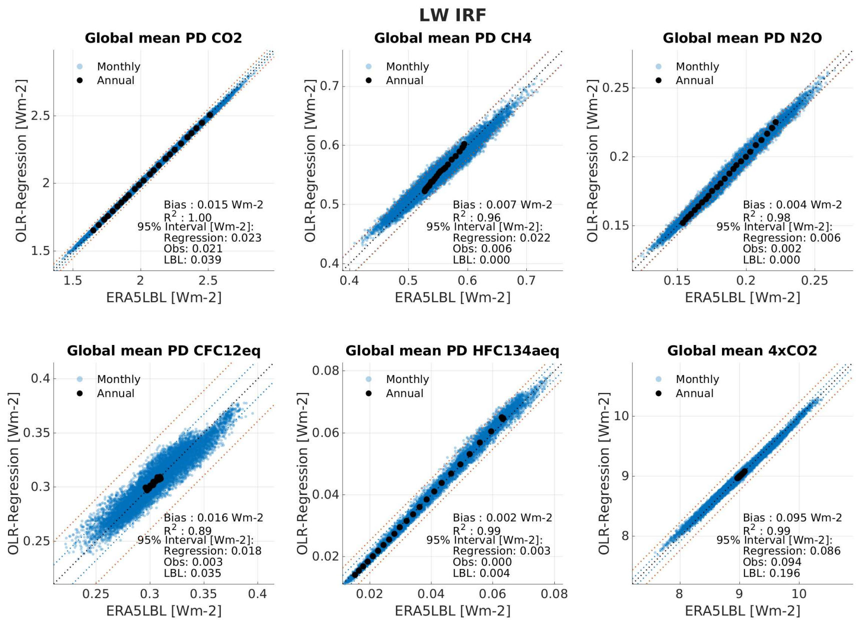

Fig. S5 Monthly meridional-mean (blue) and annual global-mean (black) LW IRF from 2001 to 2024, estimated using ERALBL (x-axis) and the OLR-regression method (y-axis) for individual WMGHG. Global-mean biases, R^2, and uncertainties from the OLR-regression method, clear-sky line-by-line calculations, and observation of OLR, are marked in each panel.

on Climate Change 659–740 (Cambridge University Press, Cambridge, United Kingdom and New York, NY, USA, 2013). URL https://www.ipcc.ch/report/ar5/wg1/.

[6] Ramaswamy, V. *et al.* Radiative forcing of climate: The historical evolution of the radiative forcing concept, the forcing agents and their quantification, and applications. *Meteorological Monographs* **59**, 14–1 (2019).

[7] Forster, P. *et al.* in *The earth's energy budget, climate feedbacks, and climate sensitivity. in climate change 2021: The physical science basis* (Cambridge University Press, 2021).

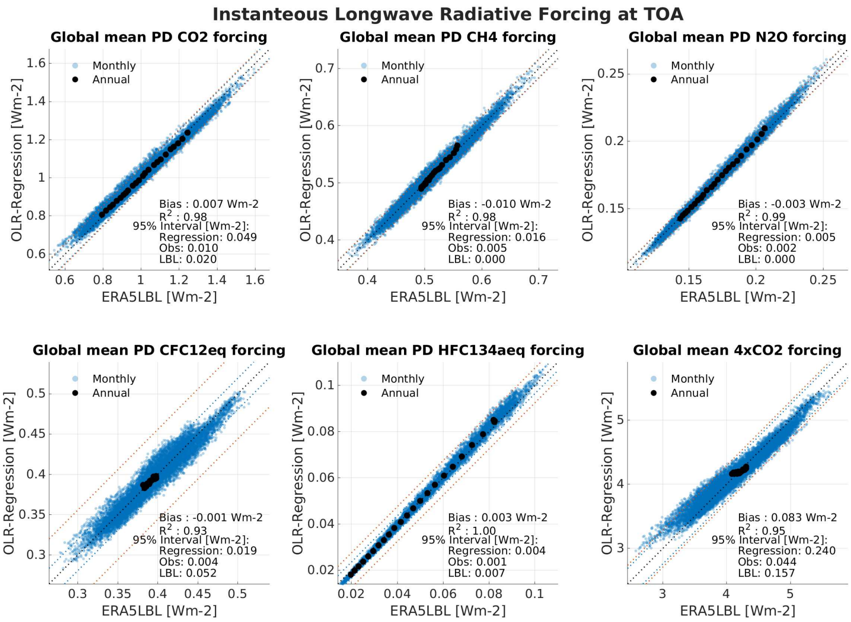

Fig. S6 Same as Fig.S5 for LW IRF at TOA.

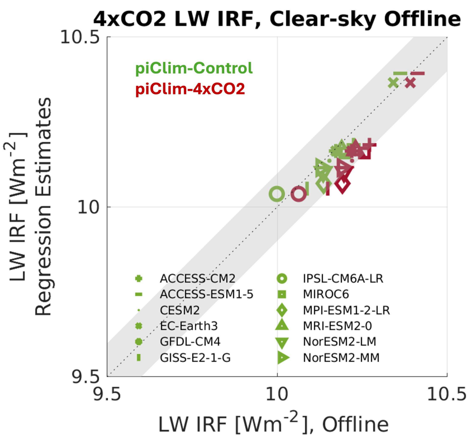

Fig. S7 The same as Figure 3(b) except that offline radiation calculations from RTE-RRTMGP driven by background states of piClim-Control and piClim-4xCO_2 experiments are compared to the OLR-regression method. The gray shading represents a 0.1 Wm^{-2} uncertainty range of the OLR-regression method when applied to 4xCO_2 LW IRF.

[8] Meinshausen, M. *et al.* Historical greenhouse gas concentrations for climate modelling (cmip6). *Geoscientific Model Development* **10**, 2057–2116 (2017).

[9] Nicholls, Z., Meinshausen, M., Pflüger, M. & Lewis, J. CMIP GHG Forcing (v1.0.0) (2025). URL https://doi.org/10.5281/zenodo.14892947.

[10] Gordon, I. E. *et al.* The hitran2016 molecular spectroscopic database. *Journal of quantitative spectroscopy and radiative transfer* **203**, 3–69 (2017).

[11] Mlynczak, M. G. *et al.* The spectroscopic foundation of radiative forcing of climate by carbon dioxide. *Geophysical research letters* **43**, 5318–5325 (2016).

[12] Byrne, B. & Goldblatt, C. Radiative forcing at high concentrations of well-mixed greenhouse gases. *Geophysical Research Letters* **41**, 152–160 (2014).

[13] Etminan, M., Myhre, G., Highwood, E. J. & Shine, K. P. Radiative forcing of carbon dioxide, methane, and nitrous oxide: A significant revision of the methane radiative forcing. *Geophysical Research Letters* **43**, 12–614 (2016).

[14] Pincus, R. *et al.* Benchmark calculations of radiative forcing by greenhouse gases. *Journal of Geophysical Research: Atmospheres* **125**, e2020JD033483 (2020).

[15] Forster, P. M. *et al.* Indicators of global climate change 2024: annual update of key indicators of the state of the climate system and human influence. *Earth System Science Data* **17**, 2641–2680 (2025).

[16] Andrews, T. & Forster, P. M. Co2 forcing induces semi-direct effects with consequences for climate feedback interpretations. *Geophysical Research Letters* **35** (2008).

[17] Zhang, M. & Huang, Y. Radiative forcing of quadrupling co2. *Journal of Climate* **27**, 2496–2508 (2014).

[18] Huang, Y., Tan, X. & Xia, Y. Inhomogeneous radiative forcing of homogeneous greenhouse gases. *Journal of Geophysical Research: Atmospheres* **121**, 2780–2789 (2016).

[19] Jeevanjee, N., Seeley, J. T., Paynter, D. & Fueglistaler, S. An analytical model for spatially varying clear-sky co 2 forcing. *Journal of Climate* **34**, 9463–9480 (2021).

[20] He, H., Kramer, R. J., Soden, B. J. & Jeevanjee, N. State dependence of co2 forcing and its implications for climate sensitivity. *Science* **382**, 1051–1056 (2023).

[21] Chen, Y.-T., Merlis, T. M. & Huang, Y. The cause of negative co2 forcing at the top-of-atmosphere: The role of stratospheric versus tropospheric temperature inversions. *Geophysical Research Letters* **51**, e2023GL106433 (2024).

[22] Forster, P. M. d. F. *et al.* Resolution of the uncertainties in the radiative forcing of hfc-134a. *Journal of Quantitative Spectroscopy and Radiative Transfer* **93**, 447–460 (2005).

[23] Myhre, G., Stordal, F., Gausemel, I., Nielsen, C. J. & Mahieu, E. Line-by-line calculations of thermal infrared radiation representative for global condition: Cfc-12 as an example. *Journal of Quantitative Spectroscopy and Radiative Transfer* **97**, 317–331 (2006).

[24] Hodnebrog, Ø. *et al.* Global warming potentials and radiative efficiencies of halocarbons and related compounds: A comprehensive review. *Reviews of Geophysics* **51**, 300–378 (2013).

[25] Maycock, A. C., Smith, C. J., Rap, A. & Rutherford, O. On the structure of instantaneous radiative forcing kernels for greenhouse gases. *Journal of the Atmospheric Sciences* **78**, 949–965 (2021).

[26] Byrom, R. E. & Shine, K. P. Methane's solar radiative forcing. *Geophysical Research Letters* **49**, e2022GL098270 (2022).

[27] Czarnecki, P., Polvani, L. & Pincus, R. Analytical models of instantaneous radiative forcing across opacity regimes. *Authorea Preprints* (2025).

[28] Koll, D. D. & Cronin, T. W. Earth's outgoing longwave radiation linear due to h2o greenhouse effect. *Proceedings of the National Academy of Sciences* **115**, 10293–10298 (2018).

[29] Feng, J., Paynter, D., Wang, C. & Menzel, R. How atmospheric humidity drives the outgoing longwave radiation–surface temperature relationship and inter-model spread. *Environmental Research Letters* **18**, 104033 (2023).

[30] Pincus, R., Hemler, R. & Klein, S. A. Using stochastically generated subcolumns to represent cloud structure in a large-scale model. *Monthly weather review* **134**, 3644–3656 (2006).

[31] Davis, S. M. *et al.* Assessment of upper tropospheric and stratospheric water vapor and ozone in reanalyses as part of s-rip. *Atmospheric chemistry and physics* **17**, 12743–12778 (2017).

[32] Wright, J. S. *et al.* Differences in tropical high clouds among reanalyses: origins and radiative impacts. *Atmospheric Chemistry and Physics* **20**, 8989–9030 (2020).

[33] Huang, H. & Huang, Y. Diagnosing the radiation biases in global climate models using radiative kernels. *Geophysical Research Letters* **50**, e2023GL103723 (2023).

[34] Smith, C. J. *et al.* Effective radiative forcing and adjustments in cmip6 models. *Atmospheric Chemistry and Physics* **20**, 9591–9618 (2020).

[35] Cess, R. *et al.* Uncertainties in carbon dioxide radiative forcing in atmospheric general circulation models. *Science* **262**, 1252–1255 (1993).

[36] Strow, L. L. & DeSouza-Machado, S. Establishment of airs climate-level radiometric stability using radiance anomaly retrievals of minor gases and sea surface temperature. *Atmospheric Measurement Techniques* **13**, 4619–4644 (2020).

[37] Teixeira, J., Wilson, R. C. & Thrastarson, H. T. Direct observational evidence from space of the effect of co 2 increase on longwave spectral radiances: the unique role of high-spectral-resolution measurements. *Atmospheric Chemistry and Physics* **24**, 6375–6383 (2024).

[38] Chen, X., Huang, X. & Strow, L. L. Near-global cfc-11 trends as observed by atmospheric infrared sounder from 2003 to 2018. *Journal of Geophysical Research: Atmospheres* **125**, e2020JD033051 (2020).

[39] Kramer, R. J. *et al.* Observational evidence of increasing global radiative forcing. *Geophysical Research Letters* **48**, e2020GL091585 (2021).

[40] Raghuraman, S. P., Paynter, D., Ramaswamy, V., Menzel, R. & Huang, X. Greenhouse gas forcing and climate feedback signatures identified in hyperspectral infrared satellite observations. *Geophysical Research Letters* **50**, e2023GL103947 (2023).

[41] Hersbach, H. *et al.* The era5 global reanalysis. *Quarterly Journal of the Royal Meteorological Society* **146**, 1999–2049 (2020).

[42] Lan, X., Tans, P., Thoning, K. *et al.* Trends in globally-averaged co2 determined from noaa global monitoring laboratory measurements. *NOAA GML* (2023).

[43] Lan, K. T., X. & Dlugokencky, E. Trends in globally-averaged ch4, n2o, and sf6 determined from noaa global monitoring laboratory measurements.version 2025-05. *NOAA GML* (2025).

[44] Ramanathan, V., Lian, M. & Cess, R. Increased atmospheric co2: Zonal and seasonal estimates of the effect on the radiation energy balance and surface temperature. *Journal of Geophysical Research: Oceans* **84**, 4949–4958 (1979).

[45] WMO. Report of the meeting of experts on potential climatic effects of ozone and other minor trace gases. Tech. Rep. (1982).

[46] Soden, B. J. *et al.* Quantifying climate feedbacks using radiative kernels. *Journal of Climate* **21**, 3504–3520 (2008).

[47] Vial, J., Dufresne, J.-L. & Bony, S. On the interpretation of inter-model spread in cmip5 climate sensitivity estimates. *Climate Dynamics* **41**, 3339–3362 (2013).

[48] Shine, K. P. & Myhre, G. The spectral nature of stratospheric temperature adjustment and its application to halocarbon radiative forcing. *Journal of Advances in Modeling Earth Systems* **12**, e2019MS001951 (2020).

[49] Shine, K. P., Byrom, R. E. & Checa-Garcia, R. Separating the shortwave and longwave components of greenhouse gas radiative forcing. *Atmospheric Science Letters* **23**, e1116 (2022).

[50] Oreopoulos, L. & Cahalan, R. F. Cloud inhomogeneity from modis. *Journal of climate* **18**, 5110–5124 (2005).

[51] Barker, H. W., Stephens, G. L. & Fu, Q. The sensitivity of domain-averaged solar fluxes to assumptions about cloud geometry. *Quarterly Journal of the Royal Meteorological Society* **125**, 2127–2152 (1999).

[52] Hogan, R. J. & Illingworth, A. J. Deriving cloud overlap statistics from radar. *Quarterly journal of the royal meteorological society* **126**, 2903–2909 (2000).

[53] Oreopoulos, L., Cho, N. & Lee, D. Revisiting cloud overlap with a merged dataset of liquid and ice cloud extinction from cloudsat and calipso. *Frontiers in Remote Sensing* **3**, 1076471 (2022).

[54] Mie, G. Beiträge zur Optik trüber Medien, speziell kolloidaler Metallösungen. *Annalen der Physik* **330**, 377–445 (1908).

[55] Mitchell, D. L. Effective diameter in radiation transfer: General definition, applications, and limitations. *Journal of the Atmospheric Sciences* **59**, 2330–2346 (2002).

[56] Feng, J., Menzel, R. & Paynter, D. Toward transparency and consistency: An open-source optics parameterization for clouds and precipitation. *Journal of Advances in Modeling Earth Systems* **17**, e2024MS004478 (2025).

[57] Loeb, N. G. *et al.* Clouds and the earth's radiant energy system (ceres) energy balanced and filled (ebaf) top-of-atmosphere (toa) edition-4.0 data product. *Journal of Climate* **31**, 895–918 (2018).

[58] Loeb, N. G. *et al.* Toward optimal closure of the earth's top-of-atmosphere radiation budget. *Journal of Climate* **22**, 748–766 (2009).

[59] Smith, C. *et al.* Understanding rapid adjustments to diverse forcing agents. *Geophysical Research Letters* **45**, 12–023 (2018).

[60] Eyring, V. *et al.* Overview of the coupled model intercomparison project phase 6 (cmip6) experimental design and organization. *Geoscientific Model Development* **9**, 1937–1958 (2016).

[61] Pincus, R., Mlawer, E. J. & Delamere, J. S. Balancing accuracy, efficiency, and flexibility in radiation calculations for dynamical models. *Journal of Advances in Modeling Earth Systems* **11**, 3074–3089 (2019).

[62] Mlawer, E. J. *et al.* Development and recent evaluation of the mt_ckd model of continuum absorption. *Philosophical Transactions of the Royal Society A: Mathematical, Physical and Engineering Sciences* **370**, 2520–2556 (2012).

[63] Clough, S. A. *et al.* Atmospheric radiative transfer modeling: A summary of the aer codes. *Journal of Quantitative Spectroscopy and Radiative Transfer* **91**, 233–244 (2005).

[64] Dudhia, A. The reference forward model (rfm). *Journal of Quantitative Spectroscopy and Radiative Transfer* **186**, 243–253 (2017).

[65] Cheruy, F., Scott, N., Armante, R., Tournier, B. & Chedin, A. Contribution to the development of radiative transfer models for high spectral resolution observations in the infrared. *Journal of Quantitative Spectroscopy and Radiative Transfer* **53**, 597–611 (1995).

[66] Buehler, S. A. *et al.* Arts, the atmospheric radiative transfer simulator–version 2.2. *Geoscientific Model Development* **11**, 1537–1556 (2018).

[67] Feng, J. & Huang, Y. Impacts of tropical cyclones on the thermodynamic conditions in the tropical tropopause layer observed by a-train satellites. *Atmospheric Chemistry and Physics* **21**, 15493–15518 (2021).

[68] Liu, L., Huang, Y. & Gyakum, J. R. Clouds reduce downwelling longwave radiation over land in a warming climate. *Nature* 1–7 (2025).

[69] Yang, P. *et al.* Spectrally consistent scattering, absorption, and polarization properties of atmospheric ice crystals at wavelengths from 0.2 to 100 μ m. *Journal of the atmospheric sciences* **70**, 330–347 (2013).

[70] Huang, Y. & Bani Shahabadi, M. Why logarithmic? a note on the dependence of radiative forcing on gas concentration. *Journal of Geophysical Research: Atmospheres* **119**, 13–683 (2014).

[71] Young, P. J., Thompson, D. W., Rosenlof, K. H., Solomon, S. & Lamarque, J.-F. The seasonal cycle and interannual variability in stratospheric temperatures and links to the brewer–dobson circulation: An analysis of msu and ssu data. *Journal of Climate* **24**, 6243–6258 (2011).

[72] Chen, Y.-T., Huang, Y. & Merlis, T. M. The global patterns of instantaneous co 2 forcing at the top of the atmosphere and the surface. *Journal of Climate* **36**, 6331–6347 (2023).